Technical Article

A domain decomposition method for the computation of land mine signatures

Abstract — Metal detectors are still the most common tool for land mine detection. Yet, their false alarm rate is extremely high as they only indicate the sheer presence of metal without using any classification until today. Therefore, the German Science Ministry funded a project in order to improve the signal analysis of existing metal detectors. Within that project network, the authors followed the goal of creating a database of synthetic mine signatures which then would be used in a classification algorithm. The numerical challenge was posed by the fact that, typically, metal objects in modern land mines are much smaller than the metal detector's coils. Therefore the computation of mine signatures requires much effort regarding the discretisation of the search scenario. Here, an efficient discretisation is reached by applying a domain decomposition method which subdivides the computational domain in sub-domains with different mesh resolution. A very fine discretisation is chosen in and closely around the metal object, especially in its skin depth layer, a coarser one around the coils of the metal detector and a very coarse one in the remaining computational domain. In the following, the domain decomposition method with Lagrange multipliers is presented for the magneto-quasistatic equations which mathematically describe the scenario of a metal detector used as a mine searching device.

I. Introduction

Based on the eddy current principle, metal detectors are able to discover buried metal objects. With the help of an acoustic signal of such a detector, a qualified mine seeker is able to determine easily the horizontal position of the detected metal object. But today's metal detectors do not enable a classification of the object with respect to its size, shape or depth. Because of that, a distinction between a mine and a harmless object is impossible for the mine seeker. In practice, only one signal in every hundred or thousand is actually caused by a mine [1].

By automatic comparison of the measured signals with predetermined signals of known configurations stored in a database, the detector could automatically sort out objects which can clearly be classified as harmless and give more detailed information about other hidden metal parts to the deminer. Thus the false alarm rate and with it the operational time could massively be lowered.

For the mine searching application, the magneto-quasistatic approach is valid. The simulation of such arrangements poses a challenge due to two points.

The first point is the high accuracy needed, resulting from the superposition of the primary field created by the metal detector and the much smaller secondary field caused by the induced eddy currents in the metal objects. A high-precision computation of the secondary field, i.e. of the difference in the fields obtained from computations with and without some metal object under the coils of the detector, can be reached by first computing the primary field only and then computing the secondary field in a second step.

The second critical point is the discretisation of the arrangement. The metal objects in mines with sizes of few millimetres are typically much smaller than the detector head with diameters of about 30 cm. Furthermore, the skin effect in the objects has to be taken into account. Typical skin depths for this application range from 0.1 mm to a few millimetres. Due to these facts, different resolutions for the meshes of the metal objects and of the detector head would be desirable. Standard methods usually produce a large number of grid points or the necessary resolution can not be reached at all.

To solve this problem, a domain decomposition method with Lagrange multipliers is used in this paper together with the Finite Integration Technique (FIT) [2], [3]. Domain decomposition implies a subdivision of the computational domain in non-overlapping sub-domains with different meshes. That gives for example the possibility to choose a fine mesh for the metal object, especially for the skin depth, a coarser one for the metal detector and a very coarse one for the rest of the computational domain. A system of equations is set up for all sub-domains. To obtain continuity for the values on the interface, the sub-domains are coupled with interface conditions using Lagrange multipliers. Altogether, this leads to a new linear system of equations which has to be solved.

The paper is organized as follows: The analytic magneto-quasistatic equations and the Finite Integration Technique are introduced in section II. Before the domain decomposition method with Lagrange multipliers is described for two sub-domains in section III, a short overview on domain decomposition is presented. The third section is closed with using the domain decomposition method with Lagrange multipliers for several sub-domains. In section IV the results are presented. There, some analytical solutions are described which are used for validation. Next, the influence of the size of the computational domain and the influence of the discretisation inside the object are given. This section ends with a comparison of the domain decomposition method with commercial software and measured signals.

II. Magneto-Quasistatic equations

A. Analytic equations

Metal detectors are based on the eddy current principle and generally consist of two coils. The transmitting coil is excited with single- or multi-frequency or with impulse signals. These currents lead to an electromagnetic field, the so-called primary field, around the metal detector. This primary field induces eddy currents in metal objects which, in turn, generate a new electromagnetic field, the so-called secondary field. This secondary field superimposes with the primary one and changes the induced voltage in the receiving coil. This change of voltage is measured and if it is high enough an acoustic signal calls the attention of the deminer to the hidden metal object.

Since the case of impulse excitation can be tackled by superposition of time harmonic excitation with different frequencies this paper deals with the time harmonic excitation.

In general, the frequencies of metal detectors for mine searching are between 1 and 50 kHz [1]. For the simulation of these arrangements, the magneto-quasistatic approach is valid for the following reasons, the wavelength is much smaller than the dimension of the computational domain and the displacement current densities are much smaller than the total current densities, so they can be neglected.

The time harmonic Maxwell's equations for magneto-quasistatics can be expressed as follows:

$$\operatorname{curl}\underline{\mathbf{E}} = -i\omega\underline{\mathbf{B}}, \tag{1}$$

$$\operatorname{curl}\underline{\mathbf{H}} = \underline{\mathbf{J}}, \tag{2}$$

$$\operatorname{div}\underline{\mathbf{D}} = \rho, \tag{3}$$

$$\operatorname{div}\underline{\mathbf{B}} = 0. \tag{4}$$

Within this system, the complex phasor of the electric field strength is denoted by $\underline{\mathbf{E}}$, the imaginary unit by i, the angular frequency by ω, the phasor of the magnetic induction by $\underline{\mathbf{B}}$, the phasor of the magnetic field strength by $\underline{\mathbf{H}}$, the phasor of the displacement current by $\underline{\mathbf{D}}$ and the source density by ρ. The phasor of the total current density $\underline{\mathbf{J}}$ arises from the sum of the conduction current density, which is the product of the conductivity σ with the phasor $\underline{\mathbf{E}}$ of the electric field strength, plus the phasor $\underline{\mathbf{J}}_E$ of the source current density, i.e.:

$$\underline{\mathbf{J}} = \sigma\underline{\mathbf{E}} + \underline{\mathbf{J}}_E. \tag{5}$$

Putting the first Maxwell's equation (1) into the second (2) and considering the formula for the total current density (5) as well as the material equation

$$\underline{\mathbf{B}} = \boldsymbol{\mu}\underline{\mathbf{H}}, \tag{6}$$

yields the magneto-quasistatic equation for the electric phasor $\underline{\mathbf{E}}$:

$$\operatorname{curl}\frac{1}{\mu}\operatorname{curl}\underline{\mathbf{E}} + i\omega\sigma\underline{\mathbf{E}} = -i\omega\underline{\mathbf{J}}_E. \tag{7}$$

Using (4), the phasor $\underline{\mathbf{B}}$ of the magnetic induction can be described as curl of the magnetic vector potential $\underline{\mathbf{A}}$:

$$\underline{\mathbf{B}} = \operatorname{curl}\underline{\mathbf{A}}. \tag{8}$$

Thus, the magneto-quasistatic equation for the magnetic vector potential $\underline{\mathbf{A}}$ results:

$$\operatorname{curl}\frac{1}{\mu}\operatorname{curl}\underline{\mathbf{A}} + i\omega\sigma\underline{\mathbf{A}} = \underline{\mathbf{J}}_E. \tag{9}$$

Equation (8) defines the magnetic vector potential only up to a gradient of a scalar function. As usual, the Coulomb gauge:

$$\operatorname{div}\underline{\mathbf{A}} = 0 \tag{10}$$

is chosen. Consequently, a grad-div term has to be added to the left hand side of (9) which yields the gauged magneto-quasistatic equation for the magnetic vector potential $\underline{\mathbf{A}}$:

$$\operatorname{curl}\frac{1}{\mu}curl\underline{\mathbf{A}} + i\omega\sigma\underline{\mathbf{A}} + \operatorname{grad}\operatorname{div}\underline{\mathbf{A}} = \underline{\mathbf{J}}_E. \tag{11}$$

This is the basic equation for the computation of mine signatures as measured by metal detectors.

B. Application of the Finite Integration Technique

Because the domain decomposition method is applied here for the Finite Integration Technique (FIT) [2], [3], this method will be briefly described. In the Finite Integration Technique the electromagnetic field quantities are mapped onto a dual grid pair. While the discrete magnetic vector potential $\hat{\mathbf{a}}$ is allocated to the primary grid edges, the discrete source currents $\hat{\tilde{\mathbf{j}}}_E$ are assigned to the dual grid facets. Furthermore, the analytical curl, gradient and divergence operators are transferred to the discrete primary and dual curl operators $\mathbf{C}$ and $\tilde{\mathbf{C}}$, to the discrete gradient operator $\tilde{\mathbf{S}}^{\mathrm{T}}$ and the discrete primary and dual divergence operators $\mathbf{S}$ and $\tilde{\mathbf{S}}$, respectively. The material parameters, the conductivity σ, permittivity ε and permeability μ, are averaged along grid facets or grid edges and collected in the matrices $\mathbf{M}_\sigma$, $\mathbf{M}_\varepsilon$ and $\mathbf{M}_{\mu^{-1}}$. With this, equation (9) can be written in the framework of FIT:

$$\left(\tilde{\mathbf{C}}\mathbf{M}_{\mu^{-1}}\mathbf{C} + i\omega\mathbf{M}_\sigma\right)\hat{\mathbf{a}} = \hat{\tilde{\mathbf{j}}}_E. \tag{12}$$

Because the Coulomb gauge is already implied in the conducting regions of the solution domain, gauging is only necessary for the non-conducting regions. Now, the diagonal matrix $\mathbf{D}_\mathrm{n}$ selects the appropriate entries in the discrete vector potential $\hat{\mathbf{a}}$ in order to enforce the Couloumb gauge only in the non-conducting regions [4]. Adding the grad-div term, the magneto-quasistatic equation is achieved in the framework of FIT:

$$\left(\tilde{\mathbf{C}}\mathbf{M}_{\mu^{-1}}\mathbf{C} + i\omega\mathbf{M}_\sigma + \frac{1}{\varepsilon_0}\mathbf{M}_\varepsilon\tilde{\mathbf{S}}^{\mathrm{T}}\mathbf{D}_\mathrm{n}\tilde{\mathbf{S}}\frac{1}{\varepsilon_0}\mathbf{M}_\varepsilon\right)\hat{\mathbf{a}} = \hat{\tilde{\mathbf{j}}}_E. \tag{13}$$

In order to simplify equations for further considerations, the system matrix $\mathbf{K}$ is defined as:

$$\mathbf{K} := \tilde{\mathbf{C}}\mathbf{M}_{\mu^{-1}}\mathbf{C} + i\omega\mathbf{M}_\sigma + \frac{1}{\varepsilon_0}\mathbf{M}_\varepsilon\tilde{\mathbf{S}}^{\mathrm{T}}\mathbf{D}_\mathrm{n}\tilde{\mathbf{S}}\frac{1}{\varepsilon_0}\mathbf{M}_\varepsilon. \tag{14}$$

C. Computing the secondary fields

In mine detection with metal detectors the change of voltage of the receiving coil is measured. The voltage change U_S originates from the secondary fields of the objects which disturb the primary field of the detector. It can be computed taking the integral of the secondary electric field strength $\underline{\mathbf{E}}_S$ or rather of the secondary magnetic vector potential $\underline{\mathbf{A}}_S$ along the receiving coil:

$$U_S = \int_S \underline{\mathbf{E}}_S ds = -\mathrm{i}\omega\int_S \underline{\mathbf{A}}_S ds. \tag{15}$$

Since the secondary field is caused by the primary one, for the computation of the secondary field the simulation of the primary is a condition. Now, two variants are possible for the computation of the secondary field. Firstly, $\underline{\mathbf{A}}_S$ may be computed as the difference of the primary vector potential $\underline{\mathbf{A}}_P$ and the superposed primary and secondary vector potential $\underline{\mathbf{A}}_{PS}$:

$$\underline{\mathbf{A}}_S = \underline{\mathbf{A}}_{PS} - \underline{\mathbf{A}}_P. \tag{16}$$

As the subtraction of these vectors with large entries but much smaller difference is not advisable because of rounding errors, the second possibility is the better choice. Here, in a first step the primary magnetic vector potential is computed:

$$\mathbf{K}_P\hat{\mathbf{a}}_P = \hat{\tilde{\mathbf{j}}}_E. \tag{17}$$

In the second step, the system of equations for the superposition of primary and secondary magnetic vector potential is set up:

$$\mathbf{K}_{PS}\hat{\mathbf{a}}_{PS} = \hat{\tilde{\mathbf{j}}}_E. \tag{18}$$

From this linear system for the computation with metal object the term $\mathbf{K}_{PS}\hat{\mathbf{a}}_P$ is subtracted from both sides. With this, the system of equations for the secondary field $\hat{\mathbf{a}}_S = \hat{\mathbf{a}}_{PS} - \hat{\mathbf{a}}_P$ is given as:

$$\mathbf{K}_{PS}\hat{\mathbf{a}}_S = \hat{\tilde{\mathbf{j}}}_E - \mathbf{K}_{PS}\hat{\mathbf{a}}_P. \tag{19}$$

Now, this system of equations is solved after computing the primary magnetic vector potential $\hat{\mathbf{a}}_P$ first.

III. Domain Decomposition

A. Overview on domain decomposition methods

In the following, a classification of the main domain decomposition methods [5], [6], [7], [8] is presented. In all these methods a subdivision of the global problem into partial problems with smaller complexity takes place [8]. Domain decomposition methods can be used for different tasks. The first one is the optimization of discretisations for numerical simulations, the second one the development of efficient solvers and the third one is parallelization [8]. In [5] another application is given with coupling different physical sizes. In practice, often more than one of these points is true.

Domain decomposition methods are classified in two groups. The first one consists of the so-called Schwarz methods like the alternate Schwarz method, multiplicative Schwarz method and the additive Schwarz method, to mention only some. The sub-domains of these methods overlap. The second group is composed of the substructure methods like the Dirichlet-Neumann method, the Mortar method or the domain decomposition method with Lagrange multipliers. These methods are also called non-overlapping methods, because their sub-domains only touch each other. The substructure methods can be classified in three different ways. The first one is the classification into direct or iterative methods, relating to the solver used. The second one subdivides the substructure methods concerning the conditions on the interface of the sub-domains. Herein, Le Tallec [9] distinguishes between primary, dual and mixed methods. The last classification regards the discretisation on the interface of the sub-domains. If, on the interface, the step width on the finer grid is an integral multiple of the step width on the coarser grid, then the method is called matching. Otherwise it is called non-matching.

B. Domain decomposition with Lagrange multipliers

As already mentioned in the introduction, an effective discretisation for mine detection scenarios is necessary. Therefore, it would be favorable to have different grids for the small metal parts of the land mines and the metal detector head. The method used here, is to subdivide the computational domain in non-overlapping sub-domains with different meshes. A similar method has already been used in [10] for an electro-quasistatic application. One advantage of this approach is the possibility to discretise both sub-domains independently from each other. This allows choosing non-matching grids for the sub-domains, as presented in Fig. 1. The domain decomposition method with Lagrange multipliers for magneto-quasistatics can be implemented in five steps. These are presented in the following for the case of two sub-domains and for the framework of FIT. After that, the method will be extended to several sub-domains.

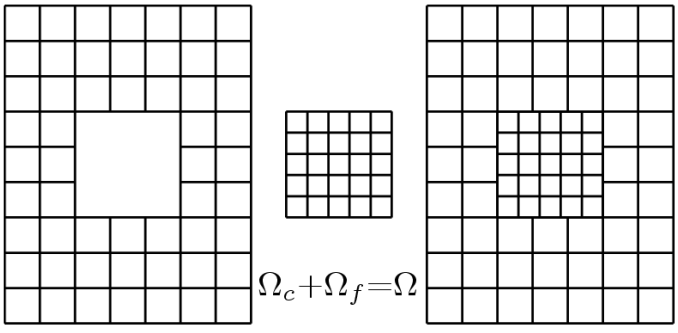

Fig. 1: Computational domain subdivided into a coarse and a fine domain.

Subdivision of the computational domain

In the first step of the implementation of the domain decomposition method with Lagrange multipliers the computational domain is subdivided into non-overlapping sub-domains. The choice of the size and position of the sub-domains depends on the requirements of the discretisation. For the mine detection scenarios, for example, one sub-domain with a fine mesh is chosen around the land mine and another one with a coarser mesh for the rest. As shown in Fig. 1, the meshes of both sub-domains can be chosen independently, which means that the coarse and the fine grid points do not need to match each other. Combining both sub-domains, the following point has to be paid regard to: The grid points of the outer sub-domain which lay in the region of the other sub-domain have to be deleted such that a sub-domain with a hole results as depicted in Fig. 1. While all terms referring to the sub-domain with fine discretisation will be denoted with subscript f, the sub-domain with the coarser grid gets the subscript *c*.

Set-up of systems of equations for the sub-domains

For both sub-domains, the magneto-quasistatic equation has to be set up. In this context, the requested boundary conditions, e.g. Dirichlet or Neumann boundary conditions, for the overall problem will be attributed to the outer boundaries of the computational domain while Neumann boundary conditions are assigned to the interface between both sub-domains. This has the advantage, that the system of equations is not influenced. The implementation of the interface conditions will be described later. Regard the sub-domains Ω_f and Ω_c. For both sub-domains, the magneto-quasistatic equations read as:

$$\mathbf{K}_\mathbf{f}\widehat{\mathbf{a}}_\mathbf{f} = \widehat{\widetilde{\mathbf{j}}}_{E,\mathbf{f}}, \tag{20}$$

$$\mathbf{K}_\mathbf{c}\widehat{\mathbf{a}}_\mathbf{c} = \widehat{\widetilde{\mathbf{j}}}_{E,\mathbf{c}}. \tag{21}$$

As described in the last section, it can be happen that one sub-domain has a hole. That means that the grid points which overlap with another sub-domain have to be deleted. Consequently, the dual grid has to be shortened to the interface for this sub-domain. If there are different materials on both sides of the interface, a correction of the averaging of the material parameters becomes necessary. For further details, see [11].

Interface conditions

The systems of equations of the sub-domains are coupled with the help of two interface conditions. They have an effect only to the values of the interface Γ and guarantee the communication between the sub-domains. These interface conditions correspond to Dirichlet or Neumann boundary conditions.

The first of two interface conditions equals a Dirichlet boundary condition, i.e. the magnetic vector potentials of both sub-domains have to be equal on the interface Γ:

$$\underline{\mathbf{A}}_c = \underline{\mathbf{A}}_f \quad \text{on } \Gamma. \tag{22}$$

Implementation of this interface condition requires the choice of the grid points situated on the interface, which is done with the selection operators $\mathbf{Q}_f$ for the fine grid and $\mathbf{Q}_c$ for the coarse grid, so that:

$$\widehat{\mathbf{a}}_{\mathbf{f},\Gamma} = \mathbf{Q}_\mathbf{f}\widehat{\mathbf{a}}_\mathbf{f}, \tag{23}$$

$$\widehat{\mathbf{a}}_{\mathbf{c},\Gamma} = \mathbf{Q}_\mathbf{c}\widehat{\mathbf{a}}_\mathbf{c}. \tag{24}$$

The dimension of the selection operators depends on the number of grid points of the sub-domain and on the number of grid points on the interface. The respective selection operator

gets entry one, if the point of the sub-domain corresponds with the point on the interface. In the other case, it gets the entry zero. The interface gets the same discretisation as the fine sub-domain so that the interface values of only one domain have to

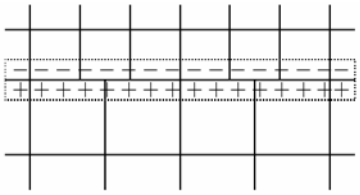

Fig. 2: Virtual current densities on the interface.

be interpolated which is necessary since the grids are non-matching. Hence, a prolongation operator $\mathbf{P}:\Gamma_c \rightarrow \Gamma_f$ is introduced which interpolates the magnetic vector potential $\hat{\mathbf{a}}_c$ of the coarse sub-domain to that one ($\hat{\mathbf{a}}_f$) of the fine sub-domain. The factors in front of the magnetic vector potential $\hat{\mathbf{a}}_c$ are stored in the prolongation operator **P**. Thus, the first interface condition reads as:

$$\mathbf{P}\mathbf{Q}_\mathbf{c}\hat{\mathbf{a}}_\mathbf{c} - \mathbf{Q}_\mathbf{f}\hat{\mathbf{a}}_\mathbf{f} = \mathbf{0}. \tag{25}$$

The second interface condition is equivalent to inhomogeneous Neumann boundary condition:

$$\frac{1}{\mu}\operatorname{curl}\underline{\mathbf{A}} = \underline{\mathbf{J}}_\Gamma \quad \text{on} \quad \Gamma. \tag{26}$$

To enforce continuity, the virtual current densities on both sides of the interface, as presented in Fig. 2, have to vanish if both grids are joint.

Because of the non-matching grids, again an interpolation for the values of one grid side is needed. The interpolation onto the magnetic vector potential $\hat{\mathbf{a}}_c$ of the coarse sub-domain is done with the restriction operator $\mathbf{P}^\mathbf{T}$ chosen as the transpose of the prolongation operator **P**. This has the advantage that the resulting system of equations described later is symmetric. Thus, the second interface condition reads as:

$$\hat{\hat{\mathbf{j}}}_{\Gamma,\mathbf{c}} = -\mathbf{P}^T\hat{\hat{\mathbf{j}}}_{\Gamma,\mathbf{f}} = \mathbf{P}^T\boldsymbol{\lambda}. \tag{27}$$

In the following, the negative discrete currents serve as Lagrange multipliers λ, which are introduced as additional unknowns to the system of equations.

The saddle point system

Since the properties of the resulting linear system of equations are of central importance for its solution they are described here besides its set-up. Combining the magneto-quasistatic equations of both sub-domains (20) and (21) plus the interface conditions (25) and (27), the system of equations for the whole computational domain reads as:

$$\begin{pmatrix} \mathbf{K}_\mathbf{c} & \mathbf{0} & \mathbf{Q}_\mathbf{c}^\mathbf{T}\mathbf{P}^\mathbf{T} \\ \mathbf{0} & \mathbf{K}_\mathbf{f} & -\mathbf{Q}_\mathbf{f}^\mathbf{T} \\ \mathbf{P}\mathbf{Q}_\mathbf{c} & -\mathbf{Q}_\mathbf{f} & \mathbf{0} \end{pmatrix} \begin{pmatrix} \hat{\mathbf{a}}_\mathbf{c} \\ \hat{\mathbf{a}}_\mathbf{f} \\ \boldsymbol{\lambda} \end{pmatrix} = \begin{pmatrix} \hat{\hat{\mathbf{j}}}_{E,\mathbf{c}} \\ \hat{\hat{\mathbf{j}}}_{E,\mathbf{f}} \\ \mathbf{0} \end{pmatrix}. \tag{28}$$

Within this system, the negative virtual current densities of the fine grid side serve as Lagrange multipliers λ. With the following definitions of the matrices $\mathbf{K}_g$ and $\mathbf{B}_1$:

$$\mathbf{K}_g := \begin{pmatrix} \mathbf{K}_c & \mathbf{0} \\ \mathbf{0} & \mathbf{K}_f \end{pmatrix}, \quad \mathbf{B}_1 := \begin{pmatrix} \mathbf{P}\mathbf{Q}_c & -\mathbf{Q}_f \end{pmatrix},$$

the structure of a saddle-point problem becomes obvious:

$$\begin{pmatrix} \mathbf{K}_g & \mathbf{B}_1^\mathbf{T} \\ \mathbf{B}_1 & \mathbf{0} \end{pmatrix} \begin{pmatrix} \hat{\mathbf{a}} \\ \boldsymbol{\lambda} \end{pmatrix} = \begin{pmatrix} \hat{\hat{\mathbf{j}}}_E \\ \mathbf{0} \end{pmatrix}. \tag{29}$$

This saddle point problem is large, sparse, complex and ill-conditioned. Furthermore, it is non-Hermitian, i.e.:

$$\mathbf{K}_g \neq (\mathbf{K}_g^*)^T = \mathbf{K}_g^H.$$

The eigenvalues of the system matrix in (29) are located in the positive half-space so that the matrix of the saddle-point problem is positive stable. The matrix $\mathbf{K}_g$ is the biggest sub-matrix of the saddle point system. It is symmetric and singular.

Solution of the saddle point system

The solution of the saddle point system which results from the simulation of mine detection scenarios has to be very accurate. The necessity for this high accuracy results on the one hand from the small secondary field of the metal object which superposes the primary field of the metal detector and on the other hand from the small error tolerances because a mine has clearly and safely to be detected always as mine.

In the literature, a lot of solvers for saddle point problems can be found, but only some are suitable for complex systems. Because of the size of the present saddle point system only iterative solvers seem appropriate. Direct solvers would need far too much memory. One of the main iterative solvers for saddle-point systems is the Uzawa algorithm [12]. One advantage of this solver is the reduction of the large original problem into two smaller problems so that, with the starting solution $\boldsymbol{\lambda}_0$ and the relaxation parameter ϑ, the following iteration scheme results:

$$\mathbf{K}_g\hat{\mathbf{a}}_{k+1} = \hat{\hat{\mathbf{j}}}_E - \mathbf{B}_1^T\boldsymbol{\lambda}_k \tag{30}$$

$$\boldsymbol{\lambda}_{k+1} = \boldsymbol{\lambda}_k + \vartheta\mathbf{B}_1\hat{\mathbf{a}}_{k+1}. \tag{31}$$

But the first equation of this scheme (30) is still very large. Furthermore, the convergence of this method is very slow so that it is not used here.

The related Arrow-Hurwicz [12] algorithm handles this problem by solving the following equations:

$$\hat{\mathbf{a}}_{k+1} = \hat{\mathbf{a}}_k + \alpha(\hat{\hat{\mathbf{j}}}_E - \mathbf{K}_g\hat{\mathbf{a}}_k - \mathbf{B}_1^T\boldsymbol{\lambda}_k) \tag{32}$$

$$\boldsymbol{\lambda}_{k+1} = \boldsymbol{\lambda}_k + \vartheta\mathbf{B}_1\hat{\mathbf{a}}_{k+1}. \tag{33}$$

Here, the choice of the two relaxation parameters α and ϑ is difficult. Besides that, like in the Uzawa algorithm, the convergence rate is very slow.

For this reason, a Krylov subspace solver [3], [12], [13] is used for the present saddle point system (29). Even if these solvers have not been developed especially for saddle point problems they show a good convergence behavior. From the group of Krylov-subspace solvers, one for complex and non-Hermitian systems has to be chosen here. Suitable solvers are BiCG, BiCGSTAB and QMR. For the given problem, BiCG showed to converge best. Nevertheless, BiCG should still be used together with a preconditioner.

Preconditioning can notably speed up iterative solvers. As most preconditioners for saddle point systems need a regular matrix $\mathbf{K}_g$, the application of the Augmented-Lagrangian technique [14] makes sense. This method transforms the original system of equations with singular matrix $\mathbf{K}_g$ to a new system of equation with regular matrix $\mathbf{K'}_g$ while the solution is not changed. As $\mathbf{B}_1\hat{\mathbf{a}} = \mathbf{0}$, then

$$\mathbf{B}_1^\mathbf{T}\mathbf{W}\mathbf{B}_1\hat{\mathbf{a}} = \mathbf{0} \tag{34}$$

is also valid. Here **W** is positive definite and often $\mathbf{W} = \gamma\,\mathbf{I}$ with $\gamma > 0$ is used [14]. Adding (34) to the first equation of the original saddle-point problem (29)

$$\mathbf{K}_\mathbf{g}\hat{\mathbf{a}} = (\mathbf{K}_\mathbf{g} + \mathbf{B}_1^\mathbf{T}\mathbf{W}\mathbf{B}_1)\hat{\mathbf{a}} = \mathbf{K}'_\mathbf{g}\hat{\mathbf{a}} = \hat{\hat{\mathbf{j}}}_E$$

yields the equivalent saddle-point problem:

$$\begin{pmatrix} \mathbf{K}_g' & \mathbf{B}_1^{\mathrm{T}} \\ \mathbf{B}_1 & \mathbf{0} \end{pmatrix} \begin{pmatrix} \hat{\mathbf{a}} \\ \boldsymbol{\lambda} \end{pmatrix} = \begin{pmatrix} \hat{\hat{\mathbf{j}}}_E \\ \mathbf{0} \end{pmatrix}. \tag{35}$$

Now, after using the Augmented Lagrangian technique, a preconditioner can be applied to accelerate the solution of the system of equations (35). The main preconditioning methods for saddle-point problems with non-Hermitian matrix $\mathbf{K}_g$ are Block-preconditioning [15], Constraint preconditioning [14], [15] and Hermitian/skew-Hermitian [16] preconditioning. The constraint preconditioner

$$\mathbf{P} = \begin{pmatrix} \hat{\mathbf{K}}_g' & \mathbf{B}_1^{\mathrm{T}} \\ \mathbf{B}_1 & \mathbf{0} \end{pmatrix} \tag{36}$$

achieves the best convergence acceleration. Here $\hat{\mathbf{K}}_g'$ is an approximation of $\mathbf{K'}_g$. The easiest choice of $\hat{\mathbf{K}}_g'$ is the main diagonal of $\mathbf{K'}_g$. Since the constraint preconditioner has the same (2x2) block structure it also has the same constraints. Furthermore, it can be seen that, as the original system, this preconditioner is a saddle-point problem as well, but easier to invert.

Several sub-domains

It can be practical to use more than two sub-domains with different discretisations, so for example for more than one metal object. In principle, two different possibilities can be distinguished for the combination of sub-domains. At the first, one sub-domain lies inside a second one and the third one lies again inside the second, as it is shown in Fig. 3, and the resolution of the discretisation increases from the outside to inside of the computational domain. One example for this is, if the sub-domain of the metal detector, which includes a finer sub-domain for the metal object, is surrounded by another large but much coarser sub-domain in order to minimize the influence of the outer boundaries on the electromagnetic fields as alternative to the implementation of open boundary conditions. The necessary mesh of the outermost sub-domain can be very coarse, indeed.

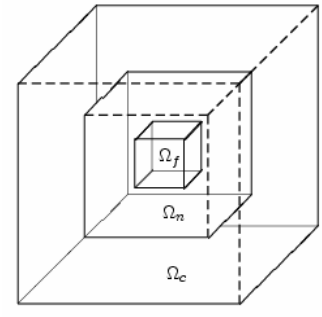

Fig. 3: Sub-domains inside each other.

The intermediate sub-domain of the described model (Fig. 3) now has two interfaces and therefore also needs two selection operators $\mathbf{Q}_{nc}$ and $\mathbf{Q}_{nf}$ as well as two prolongation operators $\mathbf{P}_{nc}$ and $\mathbf{P}_{nf}$. First, the system of equations for the interface between the coarse and the intermediate sub-domain is set up:

$$\begin{pmatrix} \mathbf{K}_c & \mathbf{0} & \mathbf{Q}_c^T \mathbf{P}_{cn}^T \\ \mathbf{0} & \mathbf{K}_{nf} & -\mathbf{Q}_{nc}^T \\ \mathbf{P}_{cn}\mathbf{Q}_c & -\mathbf{Q}_{nc} & \mathbf{0} \end{pmatrix} \begin{pmatrix} \hat{\mathbf{a}}_c \\ \hat{\mathbf{a}}_{nf} \\ \boldsymbol{\lambda}_{cn} \end{pmatrix} = \begin{pmatrix} \hat{\hat{\mathbf{j}}}_{E,c} \\ \hat{\hat{\mathbf{j}}}_{E,nf} \\ \mathbf{0} \end{pmatrix}. \tag{37}$$

The matrix $\mathbf{K}_{nf}$ and the vectors $\hat{\mathbf{a}}_{nf}$ and $\hat{\hat{\mathbf{j}}}_{E,nf}$ result from the system of equations for the interface between the intermediate and the fine sub-domain:

$$\mathbf{K}_{nf}\hat{\mathbf{a}}_{nf} = \begin{pmatrix} \mathbf{K}_n & \mathbf{0} & \mathbf{Q}_{nf}^T \mathbf{P}_{nf}^T \\ \mathbf{0} & \mathbf{K}_f & -\mathbf{Q}_f^T \\ \mathbf{P}_{nf}\mathbf{Q}_{nf} & -\mathbf{Q}_f & \mathbf{0} \end{pmatrix} \begin{pmatrix} \hat{\mathbf{a}}_n \\ \hat{\mathbf{a}}_f \\ \boldsymbol{\lambda}_{nf} \end{pmatrix} = \begin{pmatrix} \hat{\hat{\mathbf{j}}}_{E,n} \\ \hat{\hat{\mathbf{j}}}_{E,f} \\ \mathbf{0} \end{pmatrix} = \hat{\hat{\mathbf{j}}}_{E,nf}. \tag{38}$$

Inserting the system of equations (38) for the interface between intermediate and fine sub-domain into the system of equations (37) for the interface between middle and coarse sub-domain, the system of equations for the whole computational domain results:

$$\begin{pmatrix} \mathbf{K}_c & \mathbf{0} & \mathbf{0} & \mathbf{0} & \mathbf{Q}_c^T \mathbf{P}_{cn}^T \\ \mathbf{0} & \mathbf{K}_n & \mathbf{0} & \mathbf{Q}_{nf}^T \mathbf{P}_{nf}^T & -\mathbf{Q}_{nc}^T \\ \mathbf{0} & \mathbf{0} & \mathbf{K}_f & -\mathbf{Q}_f^T & \mathbf{0} \\ \mathbf{0} & \mathbf{P}_{nf}\mathbf{Q}_{nf} & -\mathbf{Q}_f & \mathbf{0} & \mathbf{0} \\ \mathbf{P}_{cn}\mathbf{Q}_c & -\mathbf{Q}_{nc} & \mathbf{0} & \mathbf{0} & \mathbf{0} \end{pmatrix} \begin{pmatrix} \hat{\mathbf{a}}_c \\ \hat{\mathbf{a}}_n \\ \hat{\mathbf{a}}_f \\ \boldsymbol{\lambda}_{nf} \\ \boldsymbol{\lambda}_{cn} \end{pmatrix} = \begin{pmatrix} \hat{\hat{\mathbf{j}}}_{E,c} \\ \hat{\hat{\mathbf{j}}}_{E,n} \\ \hat{\hat{\mathbf{j}}}_{E,f} \\ \mathbf{0} \\ \mathbf{0} \end{pmatrix}. \tag{39}$$

On closer inspection, this resulting system of equations (39) again is a saddle point problem and can also be solved as described above.

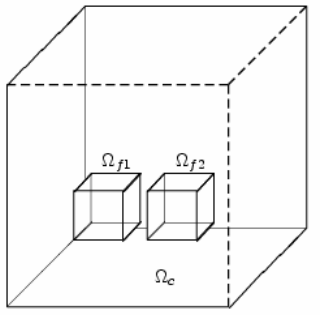

Fig. 4: Two sub-domains side by side in another one.

Another possibility of combining sub-domains is such that two sub-domains are laying side by side in a larger sub-domain as shown in Fig. 4. With this general model, a mine and another metal object under a metal detector being so far from each other that the discretisation in one sub-domain is not advisable can be computed. Under the condition that the sub-domains do not overlap, the outer sub-domain has now two different interfaces and therefore, again, two selection operators $\mathbf{Q}_{cf1}$ and $\mathbf{Q}_{cf2}$ as well as two prolongation operators $\mathbf{P}_{cf1}$ and $\mathbf{P}_{cf2}$ are needed. Neglecting for the moment the second fine sub-domain the system of equations for the coarse sub-domain Ω_c and the first fine sub-domain Ω_{f1} is set up:

$$\begin{pmatrix} \mathbf{K}_c & \mathbf{0} & \mathbf{Q}_{cf1}^T \mathbf{P}_{cf1}^T \\ \mathbf{0} & \mathbf{K}_{f1} & -\mathbf{Q}_{f1}^T \\ \mathbf{P}_{cf1}\mathbf{Q}_{cf1} & -\mathbf{Q}_{f1} & \mathbf{0} \end{pmatrix} \begin{pmatrix} \hat{\mathbf{a}}_c \\ \hat{\mathbf{a}}_{f1} \\ \boldsymbol{\lambda}_{cf1} \end{pmatrix} = \begin{pmatrix} \hat{\hat{\mathbf{j}}}_{E,c} \\ \hat{\hat{\mathbf{j}}}_{E,f1} \\ \mathbf{0} \end{pmatrix}. \tag{40}$$

In the second step the first fine sub-domain Ω_{f1} is neglected and the system of equations for the coarse sub-domain Ω_c and the second fine sub-domain Ω_{f2} is set up:

$$\begin{pmatrix} \mathbf{K}_c & \mathbf{0} & \mathbf{Q}_{cf2}^T \mathbf{P}_{cf2}^T \\ \mathbf{0} & \mathbf{K}_{f2} & -\mathbf{Q}_{f2}^T \\ \mathbf{P}_{cf2}\mathbf{Q}_{cf2} & -\mathbf{Q}_{f2} & \mathbf{0} \end{pmatrix} \begin{pmatrix} \hat{\mathbf{a}}_c \\ \hat{\mathbf{a}}_{f2} \\ \boldsymbol{\lambda}_{cf2} \end{pmatrix} = \begin{pmatrix} \hat{\hat{\mathbf{j}}}_{E,c} \\ \hat{\hat{\mathbf{j}}}_{E,f2} \\ \mathbf{0} \end{pmatrix}. \tag{41}$$

Combining and re-arranging of both systems of equations (40) and (41) leads to the system of equations for the whole computational domain:

$$\begin{pmatrix} \mathbf{K}_c & \mathbf{0} & \mathbf{0} & \mathbf{Q}_{cf1}^T\mathbf{P}_{cf1}^T & \mathbf{Q}_{cf2}^T\mathbf{P}_{cf2}^T \\ \mathbf{0} & \mathbf{K}_{f1} & \mathbf{0} & -\mathbf{Q}_{f1}^T & \mathbf{0} \\ \mathbf{0} & \mathbf{0} & \mathbf{K}_{f2} & \mathbf{0} & -\mathbf{Q}_{f2}^T \\ \mathbf{P}_{cf1}\mathbf{Q}_{cf1} & -\mathbf{Q}_{f1} & \mathbf{0} & \mathbf{0} & \mathbf{0} \\ \mathbf{P}_{cf2}\mathbf{Q}_{cf2} & \mathbf{0} & -\mathbf{Q}_{f2} & \mathbf{0} & \mathbf{0} \end{pmatrix} \begin{pmatrix} \widehat{\mathbf{a}}_c \\ \widehat{\mathbf{a}}_{f1} \\ \widehat{\mathbf{a}}_{f2} \\ \boldsymbol{\lambda}_{cf1} \\ \boldsymbol{\lambda}_{cf2} \end{pmatrix} = \begin{pmatrix} \widehat{\widehat{\mathbf{j}}}_{E,c} \\ \widehat{\widehat{\mathbf{j}}}_{E,f1} \\ \widehat{\widehat{\mathbf{j}}}_{E,f2} \\ \mathbf{0} \\ \mathbf{0} \end{pmatrix}. \quad (42)$$

On closer inspection, this is a saddle-point problem again and can be solved with the same combination of BiCG and Constraint preconditioner. Such, as many sub-domains as

seem to be appropriate can be combined. Yet, since additional Lagrange multipliers are needed on each of the new interfaces there is break-even at some point where more sub-domains would be inefficient, i.e. for each application there is an optimum between the best discretisation and the number of sub-domains.

IV. Results

Model problem with analytical solution

As model problem, circular transmitting and receiving coils both with a diameter of 30 cm are chosen. While the transmitting coil is excited with a harmonic current of 1 A and 2,400 Hz, the receiving coil can be an absolute or difference coil. The wires of both coils are assumed to be infinitely small. The metal object used here is a sphere with diameter of 2.8 cm located 20 cm below the coils.

For validation of the implemented domain decomposition method, two different analytical results can be used. The first one [17] is based on [18]. In this work, Frank assumed on the one hand that the magneto-quasistatic approach is valid and on the other hand that the conducting sphere is small enough to assume the primary field in this area to be homogenous. Based on Maxwell's equations the change of impedance is computed from the undisturbed magnetic induction, the exciting current and the current density, which are induced in the metallic sphere.

Not only conducting spheres but also permeable objects like rotational ellipsoids and a torus are treated in [19]. The authors also assume the object to be so small that the primary field of the detector is homogenous in this area. Then, the secondary field of the metal object can be obtained as dipole source. Using that dipole moment, the secondary electromagnetic fields of the metal objects are computed. Next, the voltage change can be computed by integration as given in (15).

Influence of the size of the computational domain

Even if Dirichlet boundary conditions lead to higher errors for the electromagnetic fields inside the computational domain in comparison to open boundary conditions they are used in this work because of their easy implementation. The implementation of open boundary conditions is foreseen for the future. Now, the question is studied how far the Dirichlet boundary should be put in order to get acceptable errors.

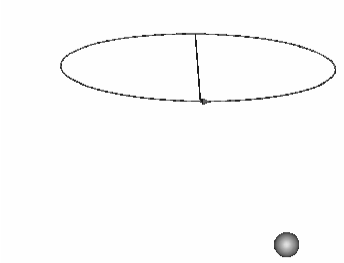

Fig. 5: Model problem

As model problem, a sphere with conductivity of $2 \cdot 10^6$ S/m is located below the metal detector, like in Fig. 5. Two models are compared: In model (A) the sphere, as part of Ω_f, gets a fine mesh with step size h_f, the metal detector, as part of Ω_n, a coarser one with step size h_n and a very coarse one with step size h_c is taken for $\Omega_c = \Omega \backslash \{\Omega_f \cup \Omega_n\}$, like in Fig. 3.. This model (A) with increasing resolution of the discretisation from outside to inside of the computational domain is compared with Model (B) with the same step widths, but only two sub-domains, one for the metal object and one for the rest.$_c$.

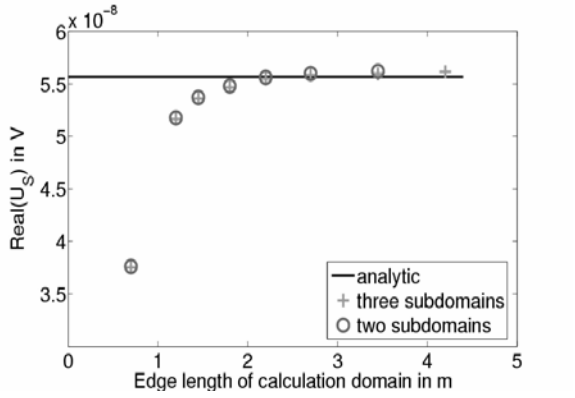

(a) Real part

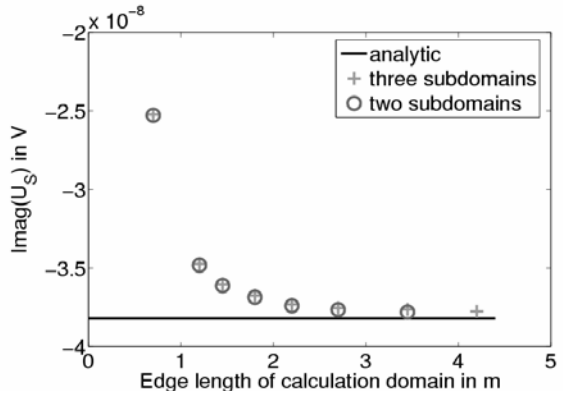

(b) Imaginary part

Fig. 6: Induced voltage change U_S as function of the size of computational domain with two and three sub-domains.

Model (A) clearly needs less grid points but the interesting point is a comparison of the computational time needed for (A) vs. (B). In Fig. 6, for both models and for the analytical solution, the induced voltage change U_S of the receiving coil is plotted as function of the size of the computational domain. In both models, increasing the computational domain leads to a better approximation of the simulated results compared to the analytic solution of [17]. For this model problem, the error reaches values below 5% for a size of 1.8 m and below 2% for a size of 2.7 m. This equals fivefold or eightfold the radius of the coil, respectively. In case of only a small space around the detector, the total computational time for model (B) is smaller than for model (A). But for a larger space around the detector and thus higher accuracy, model (A) needs less time than model (B). Thus, for the model problem presented here it makes sense to use three sub-domains. For a computational domain with size of 2.7 m this model needs only 60% of the computational time of the model with two sub-domains.

Influence of the discretisation inside the object

Since the model with three sub-domains needs less computational time than the model with two sub-domains, this model is used here. While, in the following, always the same discreti-

sations (h_n and h_c) are chosen for the sub-domains with metal detector Ω_n and the surrounding sub-domain Ω_c, the constant step width h_s within the sphere is varied.

For examination of the influence of the discretisation inside the metal objects the two cases of a sphere with the same size, but with different materials are compared: Material 1 has conductivity $\sigma_1 = 2 \cdot 10^6$ S/m and material 2 has $\sigma_2 = 2 \cdot 10^7$ S/m. Material 2 corresponds to aluminum.

In Fig. 6, for both materials, the voltage change U_S is plotted as function of the step size h_f in the sphere. The full line characterizes the analytical solution of [17], the dashed lines indicate the skin depths (δ_1=7.26 mm and δ_{alu}=2.3 mm) and 50% of the skin depths ($0.5\delta_1$=3.63 mm and $0.5\delta_{alu}$=1.15 mm), each. Fig. 7 clearly shows a convergence against the analytical solution with decreasing step size h_f. Furthermore, it can be seen that the aluminum sphere needs smaller step sizes than the sphere with the higher skin depth in order to reach the same errors. As the sphere has the same size in both cases, the different results obviously depend on the material parameters. If the same number of grid lines per skin depth is used errors of the same size are reached. For this model problem 1.5 grid lines per skin depth are mandatory for an error less than 5 % and 2 grid lines per skin depth for an error less than 2 %. As expected, for objects with the size of some centimeters as used here. The discretisation of the metal object mainly depends on the skin depth.

Comparison with commercial software

At the beginning of this project, several commercial software tools had been tested. At that time, none of the tested software was able to deliver a good discretisation and a high accuracy of the solution for these model problems representing mine searching scenarios. Meanwhile, the situation has changed.

Therefore, as an example, a comparison with the actual version of CST EM-STUDIO^{TM} [20] (CST-EMS) is presented. It allows choosing among two different mesh types – hexahedral and tetrahedral grids.

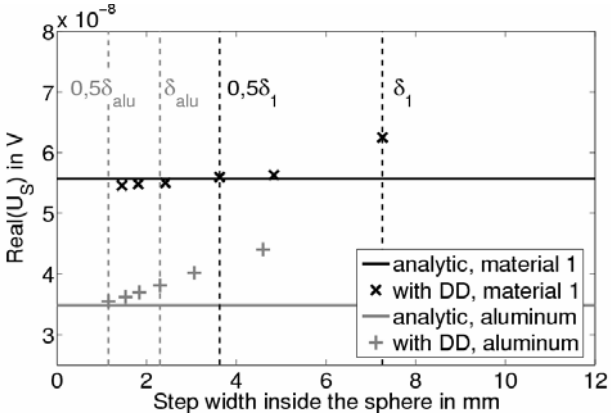

(a) Real part

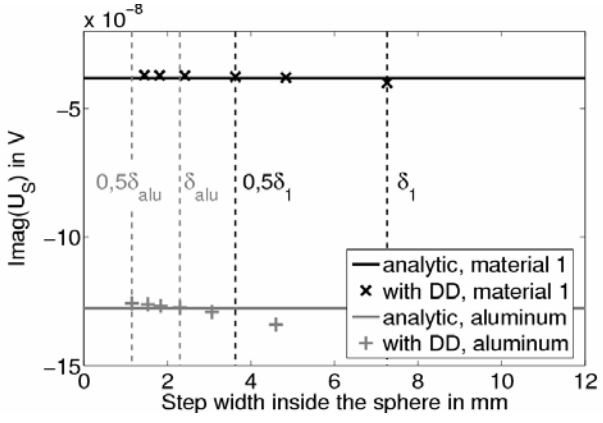

(b) Imaginary part

Fig. 7: Induced change of voltage U_S as function of the step size within the sphere, i.e. within the metal object.

The first comparison is done for the domain decomposition (DD) method with Lagrange multipliers and conventional hexahedral meshes. Therefore, again, the model problem (A) with a sphere, sub-domains Ω_f, Ω_n and Ω_c and material 1 and 2 is used. The step sizes h_n and h_c, i.e for the metal detector and the sub-domain Ω_c are kept constant for all simulations. Both, CST-EMS and DD, use conventional hexahedral grids with the same step sizes. The constant step size h_d inside the spheres is varied from computation to computation. By the topological regularity of a conventional hexahedral grid without DD, the step size h_f is automatically enforced in parts of Ω_n and Ω_c in the computations carried out by CST-EMS$_{hex}$. Thus, the number of grid points and also the memory needed in CST-EMS$_{hex}$ is larger than in the DD code. For material 1 and h_s = 3.5 mm, DD needs N_{DD} = 116,429 grid points and CST-EMS$_{hex}$ needs $N_{EMS,\ hex}$ = 428,485 grid points. This implies a factor of 3.68 for the conventional discretisation in comparison to the domain decomposition method to reach an error below 2 %. For material 2 (aluminum sphere) h_s = 1.17 mm was chosen according to the study described above. With that, DD needs N_{DD} = 142,845 grid points and CST-EMS$_{hex}$ needs $N_{EMS,\ hex}$ = 764,469 grid points. Now, the factor is 5.35 compared to DD. Clearly, with smaller skin depth, caused by higher material parameters or higher frequencies, an increasingly higher number of grid points and with it memory, can be saved using the domain decomposition method. By comparing the accuracy of the results presented in Fig. 8 a good correspondence of the results of both discretisation methods can be seen. The relative difference lies always below 2 %. With DD a significant reduction of grid points and with it of memory can be reached in comparison to conventional hexahedral meshes at similar accuracy. As the DD code is written in MATLAB only, the computational times are not optimized yet and are still very high, in fact. In future, the algorithm shall be implemented in a parallel C++ code with new solvers for the linear systems in order to reach a massive reduction in computational time as well.

For simulations with CST EM-STUDIO^{TM} also tetrahedral meshes can be chosen. The size of the elements in one area can be influenced by the maximal step size. The maximal step size of the sphere is chosen 20 times smaller than for the rest of the computational domain. Convergence studies have shown that for tetrahedral meshes in CST EM-STUDIO^{TM} about 42,000 unknowns are necessary for material 1 to achieve an error smaller than 5 % and about 260,000 unknowns for an error below 2 %. For material 2 (the aluminium sphere), however, about 84,500 unknowns are essential for an error below 5 % and about 653,500 unknowns for an error smaller than 2 %. The comparison of the mine signatures in Fig. 9 shows a better agreement to the analytical solution for the solutions of CST-EMS$_{tet}$ than with DD. To reach the same accuracy with DD as well a better discretisation has probably to be used. Yet, this would further increase the long computational time.

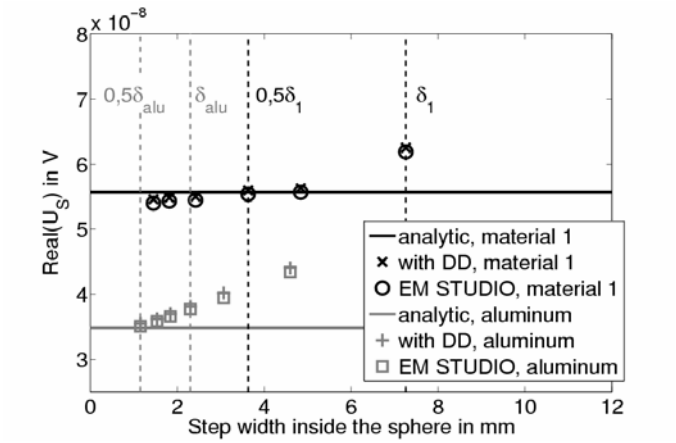

(a) Real part

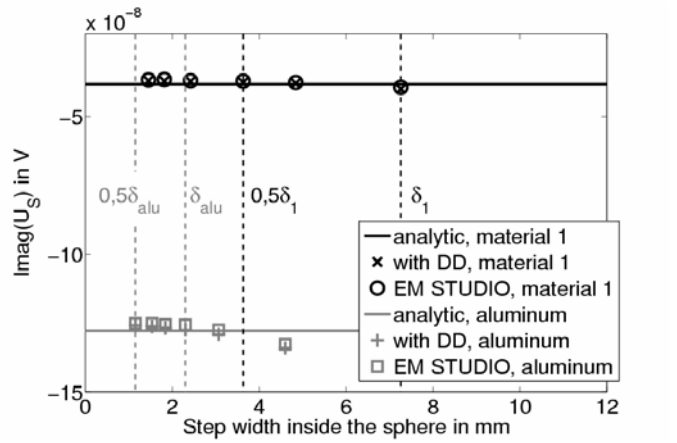

(b) Imaginary part

Fig. 8: Comparison of induced voltage change U_S computed with hexahedral grinds in CST EM STUDIO™ and domain decomposition method (DD)

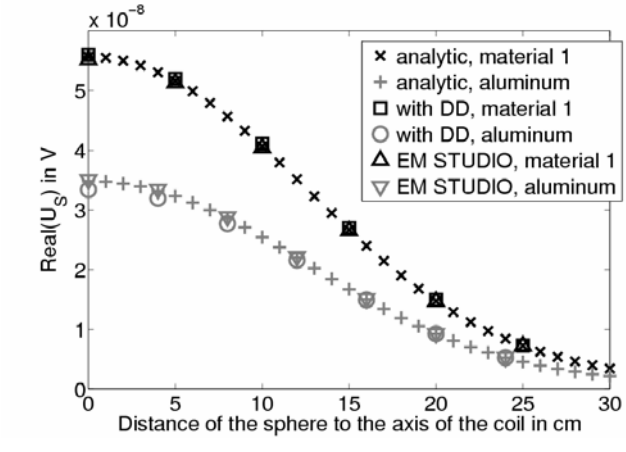

(a) Real part

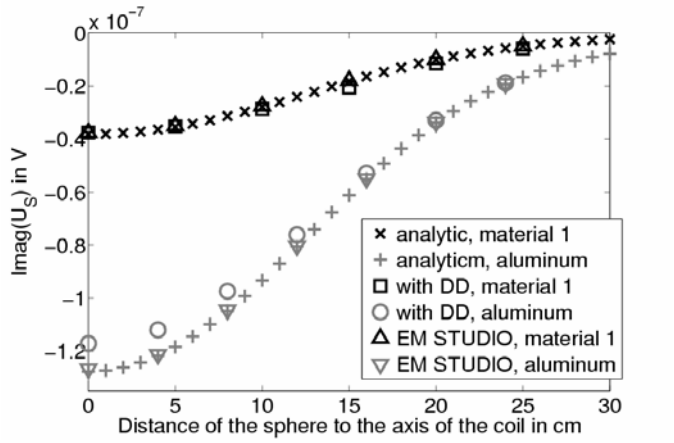

(b) Imaginary part

Fig. 9: Comparison of signatures of spheres computed with tetrahedral grids in CST EM STUDIO™ and domain decomposition method (DD).

Comparison with measured values

Measurements with the metal detector Foerster MINEX 2FD 4.500 (see also Fig. 10) carried out by Hendrik Küger [21] are used for comparison of measured signals with simulated ones.

Fig. 10: Foerster MINEX 2FD 4.500

The Foerster MINEX 2FD 4.500 is excited with harmonic currents of the frequencies 2,400 Hz and 19,000 Hz. While the transmitting unit is an absolute coil, the receiving unit is a difference coil. Both coils can be approximated by two ellipses, respectively. The biggest extension of the detector head is 22.4 cm. For the comparison, the detector is excited with a frequency of 2,400 Hz. Furthermore, an aluminium sphere with a diameter of 2.8 cm, which is located 17 cm below the coils, is used. Because of the symmetric signature, only one half one has to be computed. The model, which approximates now the detector head, is subdivided in three subdomains and has about 95,300 grid points. The gain of an amplifier of the metal detector is unknown. Therefore, this factor has to be computed. The real part of the computed voltage change at the position of 8 cm away from the center of the coils is divided by the corresponding measured value. Then, all measured values are multiplied with this factor. After this, a good agreement between the measured and the simulated signature can be seen in Fig. 1. By a similar agreement for mine signatures a lot of false alarms can be eliminated in future.

V. Conclusions

Due to the different size of the model's parts of mine detection scenarios and a high accuracy needed due to the very small secondary fields of the metal objects the simulation demands for an efficient discretisation strategy. The domain decomposition method with Lagrange multipliers presented in this paper allows a subdivision of the computational domain in non-overlapping sub-domains with independent discretisation, each. Interface conditions enforce the communication between these sub-domains. A new system of equations results at the end. This badly conditioned and complex saddle point problem is hard to be solved.

In this work a combination of BiCG and constraint preconditioner is used after the application of Augmented Lagrangian technique. For scenarios with several metal objects below a metal detector the domain decomposition method is generalized from two to several sub-domains.

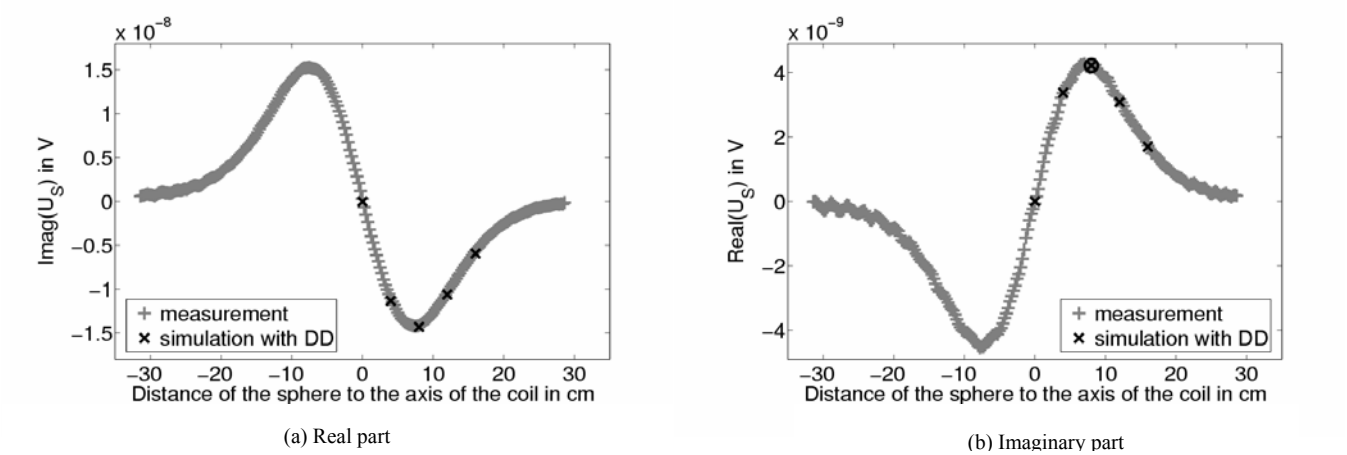

(a) Real part

(b) Imaginary part

Fig. 11: From a aluminum sphere induced change of voltage of the Foerster MINEX 2FD 4.500 in dependency of the position of the sphere

For validation, two analytical solutions from [17] and [19] were chosen. In this paper, the influence of the size of the computational domain and of the discretisation inside the metal object on the voltage change U_S was examined. It was shown that the distance between coil and outer Dirichlet boundary should be at minimum five times or better eight times the radius of the coil.

The optimal discretisation inside the object depends on the skin depth of the material. For an error below 5% at least 1.5 grid lines and below 2 % at least 2 grid lines per skin depth are necessary.

Furthermore, a comparison with actual commercial software showed the reduction of grid points and with it of memory for the domain decomposition method in comparison to conventional hexahedral meshes. Nevertheless, the results of tetrahedral meshes have better accuracies at shorter computational times. This disadvantage of the domain decomposition method which only partly has to do with the MATLAB implementation should be eliminated in future by better linear solvers.

Finally, a good agreement between the simulated results and measured ones could be shown. With the high accuracy which could be achieved for the computed results false alarms could be reduced in future.

In conclusion, further work should be devoted to the development of new solvers for the saddle point problem and to the implementation of the transient excitation in a parallel runtime-optimized code.

VI. Acknowledgment

The authors would like to thank Prof. Dr.-Ing. Herbert De Gersem, Katholieke Universiteit Leuven, and Dr.-Ing. Saku Suuriniemi, Tampere University of Technology, for helpful discussions and Dipl. Geophys. Tilman Hanstein as well as Dipl. Geophys. Jörn Löhken, University of Cologne, for the supply of the analytical solution with the dipole model.

VII. References

[1] C. Siegrist and C. Bruschini, *Metal Detectors for Humanitarian Demining: a Patent Search and Analysis.* The European Union humanitarian DEMining, May 2002.

[2] T. Weiland: *Time Domain Electromagnetic Field Computation with Finite Difference Methods.* International Journal of Numerical Modelling: Electronic Networks, Devices and Fields (NumMod), Vol. 9(4), pp. 295-319, 1996.

[3] U. van Rienen, *Numerical Methods in Computational Electrodynamics,* Vol. 12, Lecture Notes in Computational Science and Engineering, Springer, 2001.

[4] M. Clemens and T. Weiland, *Numerical algorithms for the FDiTD and FDFD simulation of slowly varying electromagnetic fields*, International Journal of Numerical Modelling: Electronic Networks, Devices and Fields, Vol. 12, pp. 3 - 22, 1999.

[5] B. F. Smith, P. E. Bjørstad and W. D. Gropp, *Domain Decomposition Parallel Multilevel Methods for Elliptic Partial Differential Equations.* Cambridge University Press, 1996.

[6] A. Toselli and O. Widlund, *Domain Decomposition Methods – Algorithms and Theory.* Vol. 34, Springer Series in Computational Mathematics. Springer, 2005.

[7] A. Quateroni and A. Valli, *Domain Decomposition Methods for Partial Differential Equations.* Numerical Mathematics and Scientific Computation. Clarendon Press Oxford, 1999.

[8] B. I. Wohlmuth, *Discretisation Methods and Iterative Solvers Based on Domain Decomposition.* Lecture Notes in Computational Science and Engineering. Springer, 2001.

[9] P. Le Tallec, *Domain decomposition methods in computational mechanics.* Computational Mechanics Advances, Vol. 1: pp. 121-220, 1994.

[10] A. Barchanski, T. Steiner, H. De Gersem, M. Clemens and T. Weiland, *Local Grid Refinement for Current Computations in 3D Human Anatomy Models*, IEEE Trans. Magn., Vol. 42, NO. 4, pp. 1371-1374, April 2006.

[11] S. Petersen, *Eine Gebietszerlegungsmethode für die numerische Berechnung elektromagnetischer Felder von Metalldetektoren für die Minensuche.* Shaker, Aachen, 2007.

[12] Y. Saad, *Iterative Methods for Sparse Linear Systems.* SIAM, ed. 2, January 2000.

[13] R. Barret et al., *Template for the Solutions of Linear Systems: Building Blocks for Iterative Methods.* SIAM, Philadelphia, 1994.

[14] M. Benzi, G. H. Golub and J. Liesen, *Numerical solution of saddle point problems.* Acta Numerica, Vol. 14, pp. 1-137, 2005.

[15] E. De Sturler and J. Liesen, *Block-Diagonal and Constraint Preconditioners for Nonsymmetric Indefinite Linear Systems Part I: Theory.* SIAM J. SCI. COMPUT., Vol. 26(5), pp. 1598-1619, 2005.

[16] M. Benzi, M. J. Gander and G. H. Golub, *Optimization of the Hermitian and skew-Hermitian splitting iteration for saddle-point problems.* BIT Numerical Mathematics, Vol. 43, pp. 881-900, 2003.

[17] H. Frank, *Vergleich von numerischer und analytischer Berechnung des elektromagnetischen Feldes einer kreisrunden Spule beeinflusst durch eine metallische Kugel.* Student project, Rostock University, January 2006.

[18] G. Hugo and S. Burke, *Impedance changes in a coil due to nearby small conducting sphere.* J. Phys. D: Appl. Phys., Vol. 21, pp. 33-38, 1988.

[19] T. Hanstein, J. Lange and S. Helwig, *Simulation unterschiedlicher Metallobjekte zur Detektion von Landminen mit Metalldetektoren.* In: O. Ritter, Eds., *Protokoll über das 21. Kolloquium Elektromagnetische Tiefenforschung.* 2005.

[20] *CST SUITE™ 2006b.* CST GmbH, Bad Nauheimer Str. 19, D-64289 Darmstadt, Germany, http://www.cst.com.

[21] H. Krüger, H. Ewald, T. Fechner and S. Bergeler, *Advanced signal processing for reduction of false alarm rate of metal detectors for humanitarian mine clearance.* In: IMTC 2006 – *Instrumentation and Measurement.* 2006.

Authors name and affiliation

Sabine Petersen and Ursula van Rienen
Institute of General Electrical Engineering
Rostock University
Albert-Einstein Str. 2
D-18051 Rostock, Germany